Article

The Mw = 5.6 Kanallaki earthquake of March 21, 2020 in west Epirus, Greece: reverse fault model from InSAR data and seismotectonic implications for Apulia-Eurasia collision

Sotiris Valkaniotis [1,*], Pierre Briole [2], Athanassios Ganas [3], Panagiotis Elias [4], Vassilis Kapetanidis [5], Varvara Tsironi [3,6], Anna Fokaefs [3], Helena Partheniou [3,5] and Panagiotis Paschos [7]

[1] Koronidos Str., 42131, Trikala, Greece; valkaniotis@yahoo.com
[2] Ecole Normale Supérieure, PSL Research University, Laboratoire de Géologie - UMR CNRS 8538, Paris, France ; briole@ens.fr
[3] National Observatory of Athens, Institute of Geodynamics, Lofos Nymfon, Thission, 11810 Athens, Greece; aganas@noa.gr; vtsironi@noa.gr; hparth83@gmail.com; anna@noa.gr
[4] National Observatory of Athens, Institute of Astronomy, Astrophysics, Space Applications and Remote Sensing, Vas. Pavlou & I. Metaxa, GR-15 236 Penteli, Greece; pelias@noa.gr
[5] National and Kapodistrian University of Athens, Department of Geology, Athens, Greece
[6] Department of Geology, University of Patras, 26504 Rio, Greece
[7] Hellenic Survey of Geology and Mineral Exploration, Unit of Epirus, 48100 Eleonas, Preveza, Greece; paschos@igme.gr
* Correspondence: valkaniotis@yahoo.com ; aganas@noa.gr Tel.: +30 210 3490186 (A.G.)

Received: date; Accepted: date; Published: date

Abstract: We identify the source of the Mw = 5.6 earthquake that hit west-central Epirus on March 21, 2020 00:49:52 UTC. We use synthetic aperture radar interferograms tied to one permanent Global Navigation Satellite System (GNSS) station (GARD). We model the source by inverting the INSAR displacement data. The inversion model suggests a shallow source on a low-angle fault (39°) dipping towards east with a centroid depth of 8.5 km. The seismic moment deduced from our model agrees with those of the published seismic moment tensors. This geometry is compatible with the Margariti thrust fault within the collision zone between Apulia and Eurasia. We also processed new GNSS data and estimate a total convergence rate between Apulia and Eurasia of 8.9 mm yr^{-1} , of which shortening of the crust between the Epirus coastal GNSS stations and station PAXO in the Ionian Sea is equivalent to ~ 50% of it or 4.6 mm yr^{-1}. A 60-km wide deformation zone takes up nearly most of the convergence between Apulia-Eurasia, trending N318°E. Its central axis runs along the southwest coast of Corfu, along the northeast coast of Paxos, heading toward the northern extremity of the Lefkada island.

Keywords: deformation; earthquake; InSAR; inversion; fault; convergence; Apulia, Epirus, Greece

1. Introduction

The tectonics of Epirus is characterised by on-going compression due to the active collision between the Apulian continental block [1,2,3,4] and the Eurasian (Aegean) plate. The Apulian continental lithosphere subducts beneath Epirus and was imaged at 70-80 km depth by [5]. Both seismological and geodetic data show that active deformation is occurring by crustal shortening directed in a NNE–SSW to NE–SW orientation [6,7,8,9,10,11] (Fig.1). The overall tectonic strain rate was estimated at 40–50 ns• yr−1 of contraction by [11] for west-central Epirus.

Preprints (www.preprints.org) | NOT PEER-REVIEWED | Posted: 27 August 2020 doi:10.20944/preprints202008.0590.v1

Geological data indicate that the region between Corfu and Ioannina (Fig. 1) is the site of Neogene thrusting and folding [2,3,12] involving mainly thin-skinned thrusting onto the Apulian margin along Triassic evaporite décollements [13]. The rock formations in most of Epirus consist of Mesozoic and Cenozoic carbonate and clastic strata of the Ionian basin of the external Hellenides belt which have been thrusted westwards onto the Apulian foreland. The inferred trace of the main basal thrust of Eurasia over Apulia, that is part of the Dinaric–Hellenic orogen, passes offshore Corfu – Paxoi islands with a general NNW–SSE orientation (Fig. 1a). In the region of Parga – Kanallaki (Fig. 1), there are two onshore thrusts of the Ionian zone running N-S and are west-directed (i.e. the Margariti and Paramithia thrusts; [14]). Offshore Parga, two west-verging reverse faults are reported by [15] (mapped on an E–W geological cross-section) to offset Pliocene–Miocene sediments, the western one representing the contact of the overthrusted Ionian zone onto the Pre-Apulian zone (Fig. 1a).

Here we use Sentinel-1 synthetic aperture radar interferograms, tied at the offsets measured at one permanent Global Navigation Satellite System (GNSS) station, to map the co-seismic displacement field of the March 21, 2020 Mw=5.6 earthquake that occurred near Kanallaki, southwest Epirus (Fig. 1c). We use the InSAR displacement data to invert for the fault parameters. Our best-fitting model is a low-angle reverse fault dipping at 39° towards the northeast. The centroid of this fault is located at a depth of 8.5 km on a structure that could be an evaporitic decollement at the base of the Ionian nappes. This finding contributes to the understanding of the present tectonic processes in the Apulia–Eurasia collision zone.

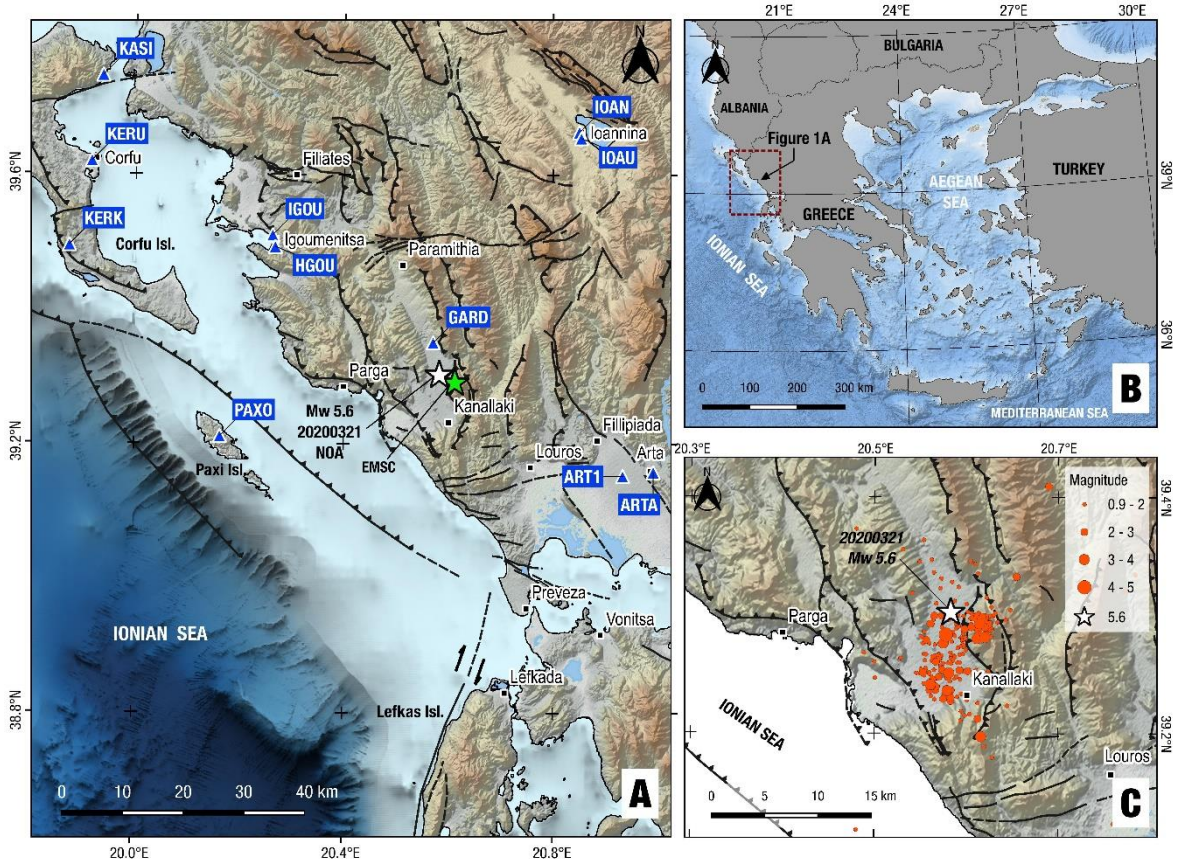

Figure 1. Map of Epirus (A) showing active fault traces (black lines with ticks on the overriding side), GNSS stations (blue triangles) and epicentres determined for the March, 21 2020 Mw=5.6 earthquake. Panel (B) shows the study area in the NW corner of Greece. Panel (C) shows the relocated epicentre of the mainshock (this study; white star) and its aftershocks (red circles; period 2020/03/20-2020/05/23). Fault traces modified after [16,17]. Black line between Paxos and Corfu islands indicates the trace of the Ionian thrust (ticks on the overriding side).

2. Seismicity

2.1 The March 21, 2020 earthquake - relocation of seismicity

On March 21, 2020 a Mw = 5.6 earthquake occurred at 00:49:52 UTC near the village of Kanallaki in Epirus (Fig. 1), 15 km East of Parga, in north-western Greece [18]. The earthquake caused damage to old houses in Kanallaki and surrounding villages (Fig. 1) but no major injuries. The mainshock was preceded by an earthquake of moderate magnitude of Mw = 4.2 on March 20th 2020 (see Table 1 for details). Until May 23, 2020 more than 280 aftershock events (with 1.0≤ML≤4.0) were recorded by the Institute of Geodynamics, National Observatory of Athens (NOAGI) of which 270 events were relocated for the purposes of this study, with horizontal location uncertainties less than 1 km (Fig. 1c; Fig. 2). The mainshock was followed by two moderate-size aftershocks, one on March 23rd and one on March 25th 2020 with magnitudes Mw = 3.8 and Mw = 3.9, respectively (Tab. 1). The moment tensor solutions of all four events indicate NW-SE reverse faulting in agreement with the regional, compressional tectonics (Tab. 1). For the mainshock, two moment tensor calculations are included in Tab. 1. The first one is based on the rapid manual solution (Fig. 3a) provided by NOA a few minutes after the earthquake occurrence. The 2nd solution of the mainshock is based on the relocated determination of its hypocentre for the needs of the present study (Fig. 3b). The calculation of the focal mechanism solutions is based on a waveform inversion methodology employing the ISOLA point source inversion software ([19]; see Fig. S1 for details on the quality of waveform fit). The crustal velocity model used for the relocated focal mechanism solution calculation was published by [20].

Table 1. Parameters and focal mechanisms of the most important events of the 2020 Kanallaki earthquake sequence (by using the ISOLA software).

dd/mm/yyyy HH:MM	Epicentre	Hypocentral Depth (km)	M_w	strike/dip/rake 1	strike/dip/rake 2	P-axis Azimuth/Plunge	T-axis Azimuth/Plunge
20/03/2020 21:38	39.3123N 20.5650E	14.7	4.2	133/56/82	328/35/102	229/10	14/77
21/03/2020 00:49	39.3265N 20.5215E	7.9	5.5	315/33/92	132/57/89	223/12	38/78
21/03/2020 00:49	39.3025N 20.5829E **(re-located)**	6.4	5.6	129/59/72	341/36/117	232/12	358/71
23/03/2020 04:41	39.3027N 20.5966E	14.1	3.8	293/60/9	199/82/149	250/15	152/27
25/03/2020 09:49	39.2757N 20.6218E	13.4	3.9	141/63/74	353/31/118	242/17	21/68

For seismicity relocation we collected catalogue and arrival-time data for the 2020 Kanallaki sequence from the online public databases of the Geodynamics Institute of the National Observatory of Athens (GI-NOA) and from the Seismological Laboratory of the National and Kapodistrian University of Athens (SL-NKUA). We merged the two databases by complementing arrival-time data for events that are common in the two catalogues and also including unique events only

 doi:10.20944/preprints202008.0590.v1

101 available on one of the two catalogues. In total, a database of 281 events was constructed for the
102 period between 1 March and 1 May 2020 in the study area. After several tests with different velocity
103 models (e.g. [20]), we adopted of the 1-D P-wave velocity model of [21] for the region of northwest
104 Greece (Table 2), which produced adequate results in terms of travel-time residuals and focal depth
105 distribution. We determined a constant ratio of Vp/Vs=1.74 using the [22] method, also considering
106 the root mean square (RMS) deviation curve with variable Vp/Vs, which presents a wide minimum
107 for Vp/Vs between 1.71 and 1.75. The mean RMS error is 0.367 s (Fig. 2a) while the average location
108 errors are ERX = 0.54 km, ERY = 0.73 km and ERZ = 2.7 km (Fig. 2b). Although the azimuthal gap is
109 relatively small for most events (mean gap = 121°; Fig. 2d), the epicentral distances from the stations
110 are, in general, larger than 30 km, which is why focal depths cannot be well constrained.

111 **Table 2.** 1-D P-wave velocity model for this region [21].

Layer	VP (km/s)	Ceiling Depth (km)
1	4.6	0.0
2	5.7	7.0
3	6.1	11.0
4	6.3	11.5
5	6.5	16.5
6	7.3	35.0
7	8.0	80.0

112

Preprints (www.preprints.org) | NOT PEER-REVIEWED | Posted: 27 August 2020 doi:10.20944/preprints202008.0590.v1

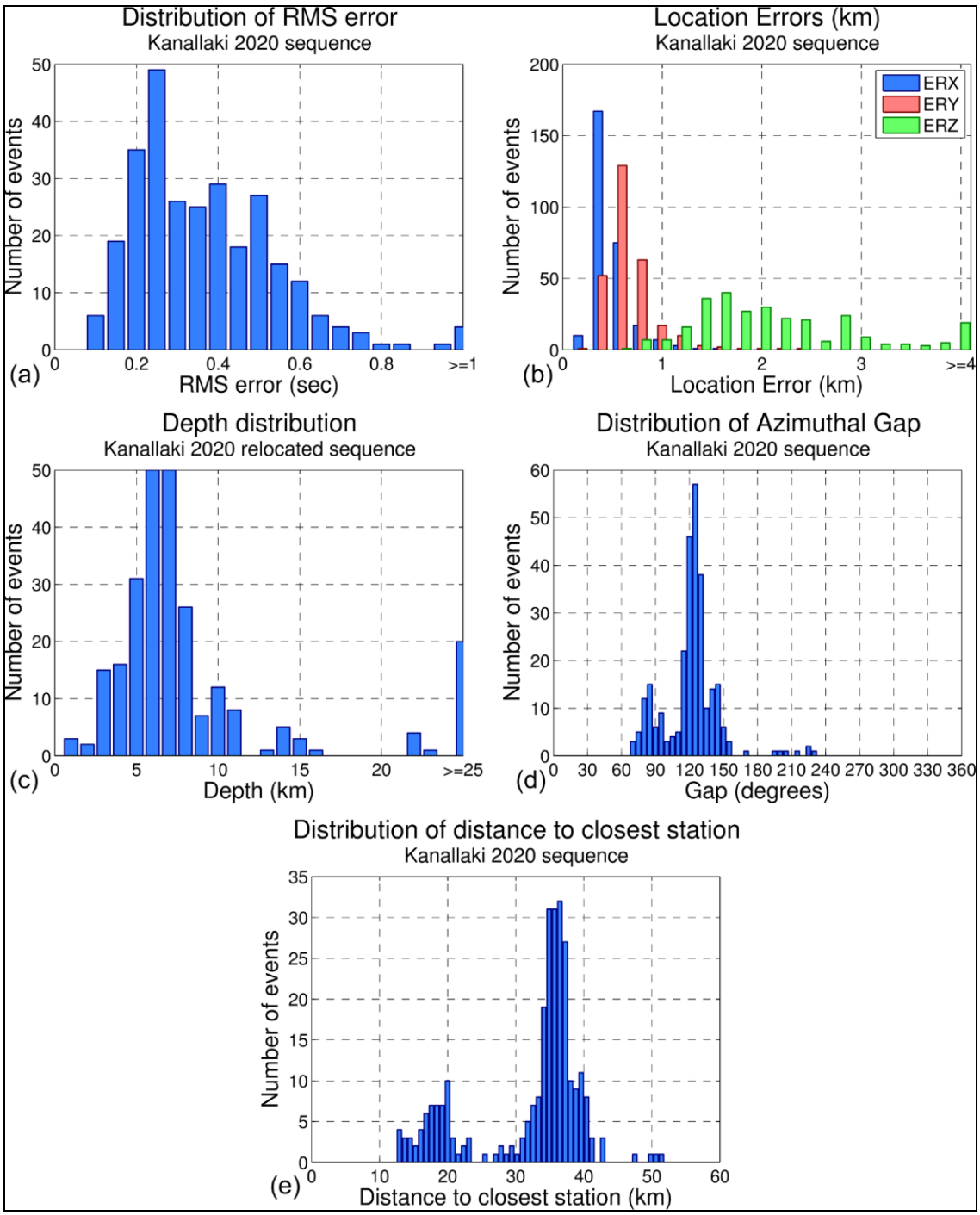

Figure 2. Distributions of location uncertainties and other statistics for the 2020 earthquake sequence in Kanallaki a) Travel-time RMS error, b) Horizontal (ERX, ERY) and vertical (ERZ) location errors, c) azimuthal gap, d) relocated focal depths and e) epicentral distance to the closest station with available arrival-time data.

To improve the hypocentral distribution we applied the double-difference relocation method using the algorithm HypoDD [23]. This method works by assuming that when the distance between two neighbouring events is much smaller than their hypocentral distance from a station, then their travel-time differences can be attributed to their inter-event distance. Relative relocation between hypocentres is achieved by minimizing the double-difference between observed and calculated travel-times for pairs of neighbouring events at common stations, reducing errors caused by unmodeled velocity structure. To further enhance the relocation procedure, we also incorporated

Preprints (www.preprints.org) | NOT PEER-REVIEWED | Posted: 27 August 2020 doi:10.20944/preprints202008.0590.v1

differential P and S travel-times from waveform cross-correlation. This creates links between strongly correlated events and reduces errors due to arrival-time reading inconsistencies. We acquired waveform data from stations of the Hellenic Unified Seismological Network from the National EIDA node (http://eida.gein.noa.gr/), hosted at GI-NOA. The relocation procedure was performed using two sets of iterations, the first with stronger a priori weights on catalogue data and the latter with higher weights on the cross-correlation data. A total of 270 events were successfully relocated (Fig. 3). The relocated focal depths are mainly distributed between 3 and 11 km. The M_w=5.6 mainshock's relocated focal depth is estimated at 6.4 km; however, it should be noted that there are significant uncertainties in the absolute focal depths due to the unavailability of data from near-field stations that cannot be corrected by double-difference relocation. Soon after the M_w=5.6 mainshock, the aftershock activity was spread to a larger region further south and to the east (Fig. 3). Cross-sections of seismicity are presented in supplementary Figure S2.

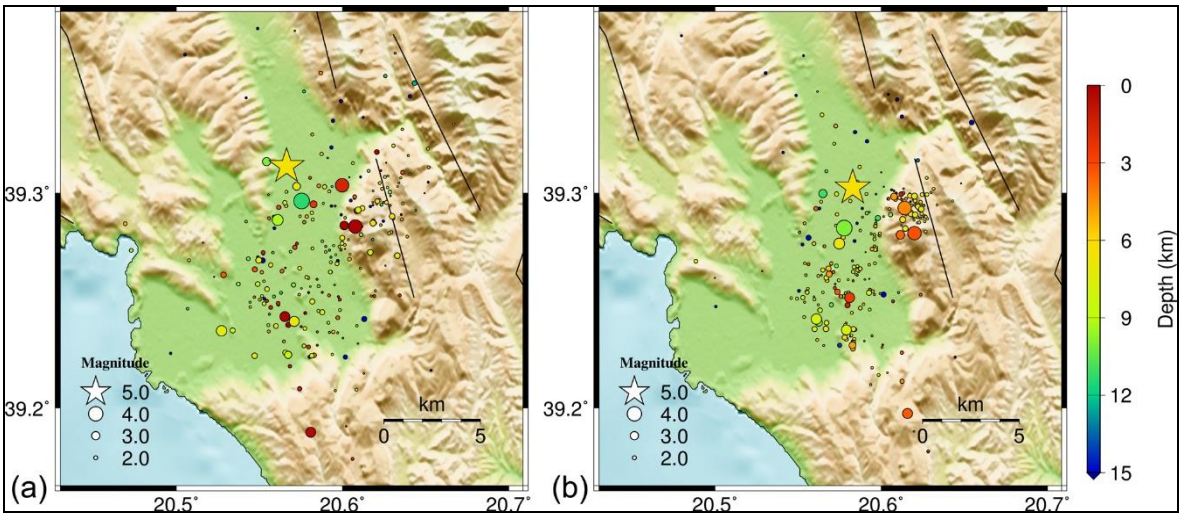

Figure 3. Relief map showing locations of epicentres (solid circles) of the 2020 Kanallaki earthquake sequence (a) before and (b) after relocation with HypoDD. Colours correspond to the focal depths. The star represents the epicentre of the M_w=5.6 mainshock of March 21, 2020.

The focal mechanism solutions produced by various agencies for the Kanallaki mainshock are reported in Tab. 3. The local agencies (NOA, AUTH) report centroid depths significantly lower than the other agencies. Our revised moment tensor solution provided a centroid depth of 8 km. We favour the east-dipping nodal plane because it fits the regional geological data (west-verging thrusts; Fig. 1c; Fig. 4). Concerning the fault strike, there are two clusters of solutions, one with NOA (initial), USGS and GFZ around N317°E and the others (GCMT, IPGP, AUTH, INGV) around N336°E. The average dip angle is 39° towards east-northeast while the average rake angle is 102°, i.e. almost pure reverse-slip.

Table 3. Focal mechanisms of the March 21, 2020 mainshock calculated by various agencies.

	Strike	Dip	Rake	Centroid depth	Moment
	°	°	°	km	* 10^{17} N m
GCMT	337	39	119	13	4.78
GFZ	318	37	90	16	4.10
IPGP	331	35	100	10	6.61
USGS	317	51	87	14	4.04
NOA	315	33	92	8	2.38
NOA revised (this study)	341	36	117	8	2.86

AUTH	336	38	105	7	3.82
INGV	333	42	107	14	4.80
average	**329**	**39**	**102**	**11**	
standard deviation	9	5	10	3.2	

151

152 *2.2 Historical Seismicity and the 1895 event*

153 The Kanallaki region is an area of relatively low seismicity in Greece where strong earthquakes
154 are rare and occur with magnitudes M < 6.0 (Fig. 4; see Table S1 for the record 1915-2019); however,
155 one disastrous earthquake has occurred in the 19th century. [24] and [25] report information on the
156 occurrence of a major M = 6.3 earthquake on May 14, 1895 at 20.61°E, 39.42°N near the village
157 Dragani ([25]; Fig. 4), 15 km north of the Kanallaki. [24] report the village Dragoumi (mod.
158 Zervohori) as the location of heaviest damage, however contemporary sources (Greek newspaper
159 "Voice of Epirus", 19/5/1895 – accessed at July 2020 through the digital archives of the Greek
160 Parliament) and [25] mention the village Dragani (mod. Ampelia) as the meizoseismal area.
161 According to the sources, the earthquake destroyed also the village Karvounari (Fig. 4) and
162 damaged several others, killing in total almost 100 people. We identified all settlements mentioned
163 in the original sources with reported damages, and plot them on a map (Fig. 4); an approximate
164 location of the 1895 rupture can be visualised by the damage distribution (dotted red ellipse in Fig.
165 4). Both approximate location of the rupture and damage distribution are compatible with a M6+
166 magnitude reverse rupture along the Margariti thrust (east-dipping), as the 1895 damage zone is
167 located on the hangingwall of this active fault. The main shock was preceded by a strong foreshock
168 on the previous day (see the catalogue of the Aristotle University of Thessaloniki at
169 http://geophysics.geo.auth.gr/ss/CATALOGS/seiscat.dat).
170
171 Moreover, on June 16, 1990 02:16 UTC an offshore M = 5.5 event occurred, that was studied by
172 [8] who determined a reverse focal mechanism. That earthquake was localized at 20.54°E, 39.16°N
173 (see Fig. 4), thus ~15 km to the southwest of the 2020 event with a centroid depth 8.5 ± 4 km, with
174 strike, dip and rake angles 352° ± 20°, 37° ± 9°, 110° ± 15° respectively, and a seismic moment of
175 $2.49 \bullet 10^{17}$ N-m. The focal mechanism and magnitude of that 1990 event are thus comparable to those
176 of the 2020 earthquake.

Preprints (www.preprints.org) | NOT PEER-REVIEWED | Posted: 27 August 2020 doi:10.20944/preprints202008.0590.v1

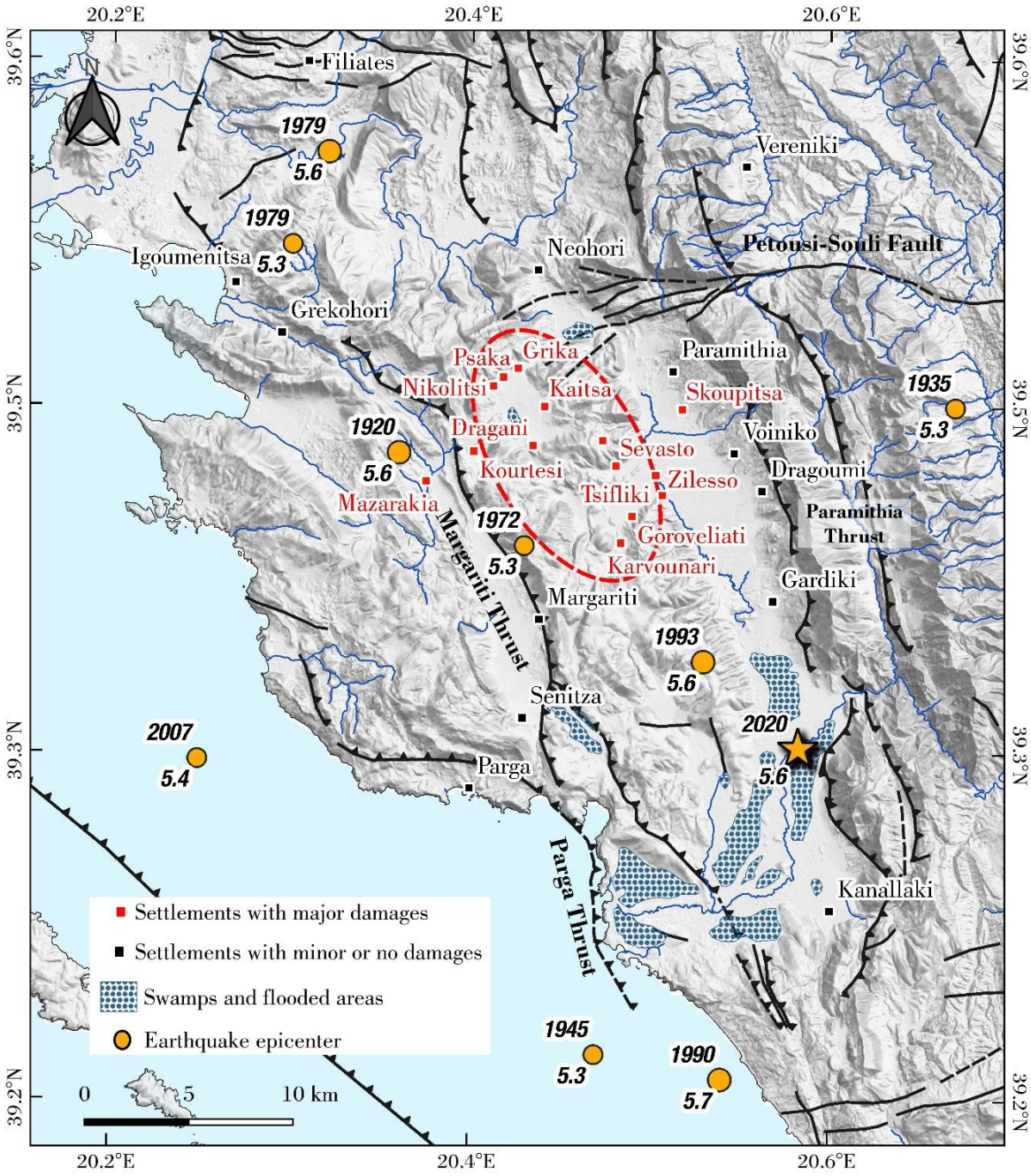

Figure 4. Map of west Epirus showing active fault traces (black lines with ticks on the overriding side (modified after [16,17] and the epicentral area of the 1895 event (red ellipse). The instrumental seismicity for Mw > 5.2 [26] is shown as solid circles. Dotted blue areas mark swamps and flooded fluvial areas during early 20th century, while settlement names used are the original ones mentioned in the 1895 earthquake reports.

3 Geodesy

3.1 Interferograms

We use synthetic aperture radar interferometry (InSAR) to capture the deformation produced by the earthquake (Fig. 5; Fig. 6). In the broader Aegean area, InSAR is systematically used to map the ground deformation produced by large earthquakes after removing the signal from the

topography [27,28,29,30,31,32,33] and minimising the effect of decorrelation factors such as tropospheric noise.

We use the Sentinel-1 descending interferogram made with the March 12 and March 24, 2020 scenes acquired on the track 153 (Fig. 5), and the ascending interferogram made with the March 19 and March 31, 2020 scenes acquired on the track 175 (Fig. 6). The quality of the descending interferogram (track 153) is exceptional with high coherence and low tropospheric disturbances. The quality of the ascending interferogram is also good. We also processed several interferograms of overlapping tracks (see Fig. S3 for ground coverage), however, the quality of the extracted information was less good (see Fig. S4 for results of unused interferograms). The unit vectors from the ground to the satellites are [-0.098, 0.504, 0.858] and [-0.105, -0.569, 0.816] in the east, north and up components for the descending and ascending views, respectively. The interferograms were produced on the Geohazards Exploitation Platform (https://geohazards-tep.eu) using the DIAPASON module of the TRE-ALTAMIRA.

The two interferograms capture the ground motion along two opposite line of sights (l.o.s.). It is these measurements of l.o.s. that we are going to model to retrieve the parameters of the fault. The digital elevation model (DEM) used for the processing is the Shuttle Radar Topography Mission (SRTM) 1 Arc-Second Global (Digital Object Identifier number: /10.5066/F7PR7TFT). We enhanced the signal to noise ratio of the interferograms by applying the adaptive power spectrum filter of [34] with a coherence threshold of 0.3.

Two moderate-size aftershocks occurred during the 4-day period following the mainshock, one on March 23 with magnitude $M_{w(NOA)} = 3.8$, the other on March 25 with magnitude $M_{w(NOA)}=3.9$ (see Tab. 1 and https://bbnet.gein.noa.gr/HL/). Because of their weak magnitudes, they are not expected to affect the deformation signal. There was also a significant foreshock of magnitude $M_{w(NOA)} = 4.2$ on March 20 21:38 UTC (Table 1), nor it is expected to have produced any measurable surface deformation.

Preprints (www.preprints.org) | NOT PEER-REVIEWED | Posted: 27 August 2020 doi:10.20944/preprints202008.0590.v1

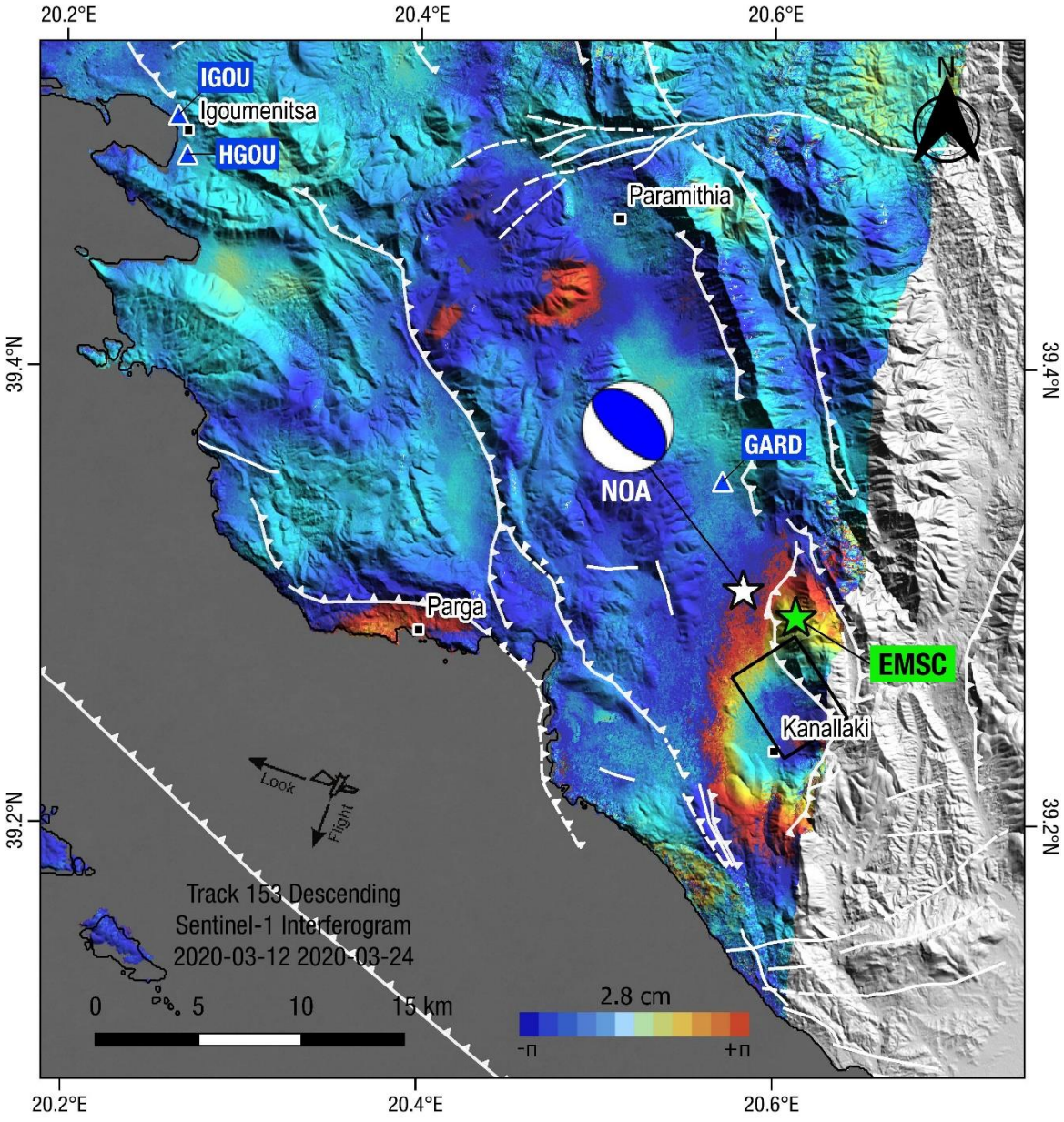

Figure 5. Descending interferogram using DIAPASON on the ESA-GEP web service platform. Solid stars indicate earthquake epicentres (green for EMSC, white for NOA relocated). Black rectangle is the preferred fault model from the geodetic inversion. Beachball indicates the NOA focal mechanism (moment tensor solution; compressional quadrant is shown in blue). White lines are active faults (ticks on the upthrown side). Colour scale (2π) shows one cycle of phase difference between a pair of images relative to the satellite (line-of-sight). A displacement fringe of at least 2.8 cm along the satellite line of sight is observed in the wider Kanallaki area.

Preprints (www.preprints.org) | NOT PEER-REVIEWED | Posted: 27 August 2020 doi:10.20944/preprints202008.0590.v1

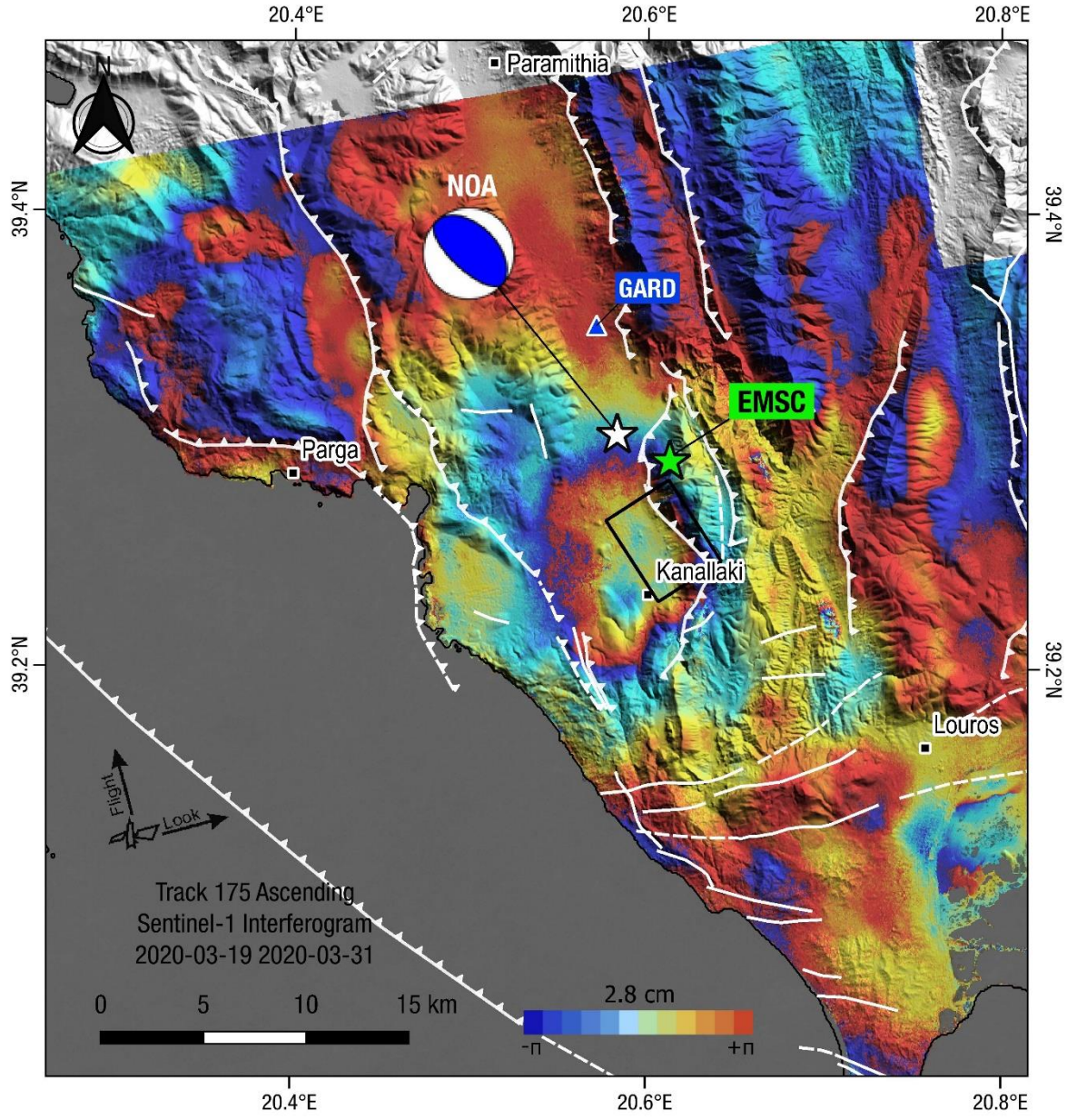

Figure 6. Ascending interferogram using DIAPASON on the ESA-GEP platform. Solid stars indicate earthquake epicentres. (green for EMSC, white for NOA relocated). Black rectangle is the preferred fault model from the geodetic inversion. Beachball indicates the NOA focal mechanism (moment tensor solution; compressional quadrant is shown in blue). White lines are active faults (ticks on the upthrown side).

3.2 Geodetic data inversion: Picking quarter of fringes

On the two above interferograms we extracted numerically by manual picking the pixels constituting the fringe with values 32, 96, 160 and 224. On the descending interferogram (see Tab. 4) we selected 86 values among 247, and on the ascending interferogram (see Table 5) 86 among 289. As expected, there are less pixels for the larger displacements as this corresponds (by definition) to smaller areas. On the descending interferogram (Fig. 5), the zero value of the interferogram is very well constrained due to the high coherence of the interferogram. We assume that the zero value is the average zero counted in the triangle Parga – Igoumenitsa – Paramithia (see Fig. 4 for locations). This assumption is justified by the non-detectable offset at the position time-series of the GNSS station GARD (Gardiki) which is located in the SW side of the tringle (see Fig. 1 for its location). The

 doi:10.20944/preprints202008.0590.v1

uncertainty is around 1/8 of a fringe, i.e. 3.5 mm in the l.o.s. Tab. 6 shows how the output of our modelling changes when changing by 1/8 of a fringe the zero of our fringes which is equivalent to changing of the same amount the maximum l.o.s. displacement, here 28 to 31.5 mm. This test is made for a descending interferogram case and with strike, dip and rake angles of 329°, 39°, 102°. The test shows that changing the zero of the interferogram by 1/8 of a fringe (3.5 mm) results in the change of the moment tensor by 32%, here completely absorbed by the increase of the fault length as this is the only free geometric parameter, the other free parameters being the three coordinates of the fault-top centre. As our first models predicted a geodetic moment slightly lower that the seismic moment (see Table S3), we use for the zero of the fringes the value that maximizes the interferogram, thus the case of maximum line of sight change of 31.5 mm.

The ascending interferogram (Fig. 6) is noisier and therefore its zero more difficult to establish. We therefore used a different method and performed the fringe tuning by aligning the geodetic moment predicted for the descending interferogram with the one predicted for the ascending one. The best fit is obtained when using 34 mm for the displacement on the top quarter of fringe of the ascending interferogram. The fault model is now made with joint inversion of the l.o.s ground motions measured with descending and ascending Sentinel-1 interferograms. Our geodetic data provided us with a robust model, and in particular on a) the 3D location of the fault-top centre b) fault length and width and c) amount of slip.

Table 4. Picked values of the descending interferogram. See Fig. 7 for locations.

Pixel value	Number of available pixels	Number of selected pixels	Displacement in the line of sight (mm)
32	161	18	31.5
96	25	19	24.4
160	24	21	17.5
224	37	28	10.5
Total	247	86	

Table 5. Picked values on the ascending interferogram. See Fig. 7 for locations.

Pixel value	Number of available pixels	Number of selected pixels	Displacement in the line of sight (mm)
96	6	6	34
160	24	20	27
224	42	20	20
32	40	20	13
96	177	20	6
Total	289	86	

Table 6. Range of variation of the 3-D location of fault-top centre, geodetic moment tensor and fault length when changing the zero value of the interferogram.

Max. l.o.s. change				Fault length	Geodetic moment tensor
	Easting	Northing	Depth		* 10^{17} N m
	km	km	km	km	
28 mm	465.45	4344.38	7.29	4.32	2.27
31.5 mm	465.44	4344.41	7.99	5.7	2.99

Preprints (www.preprints.org) | NOT PEER-REVIEWED | Posted: 27 August 2020 doi:10.20944/preprints202008.0590.v1

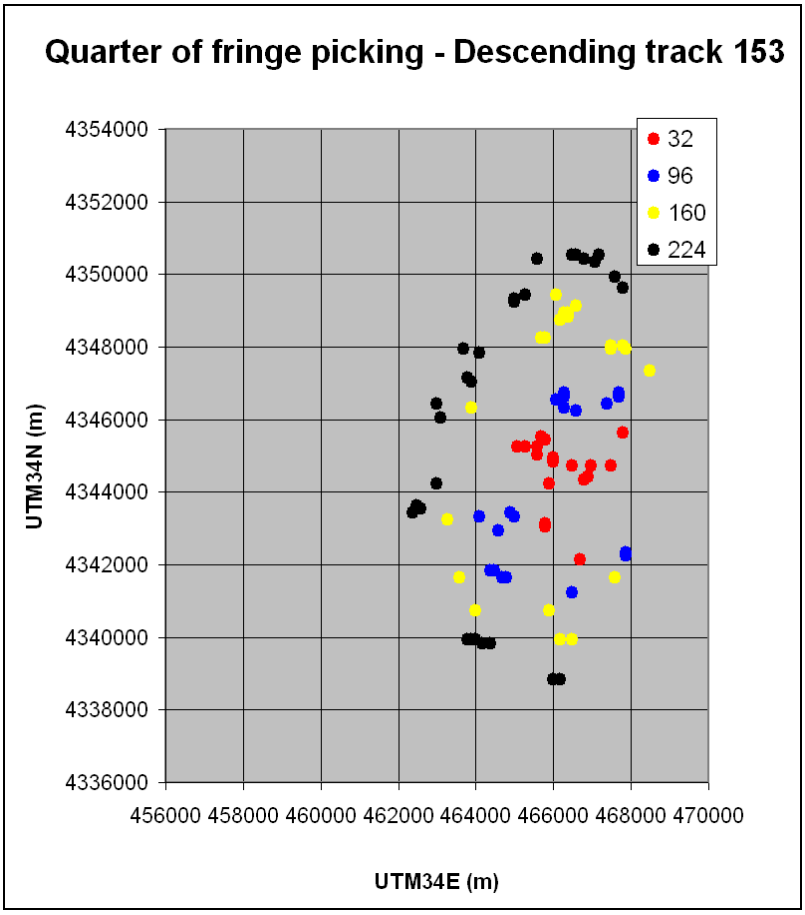

269

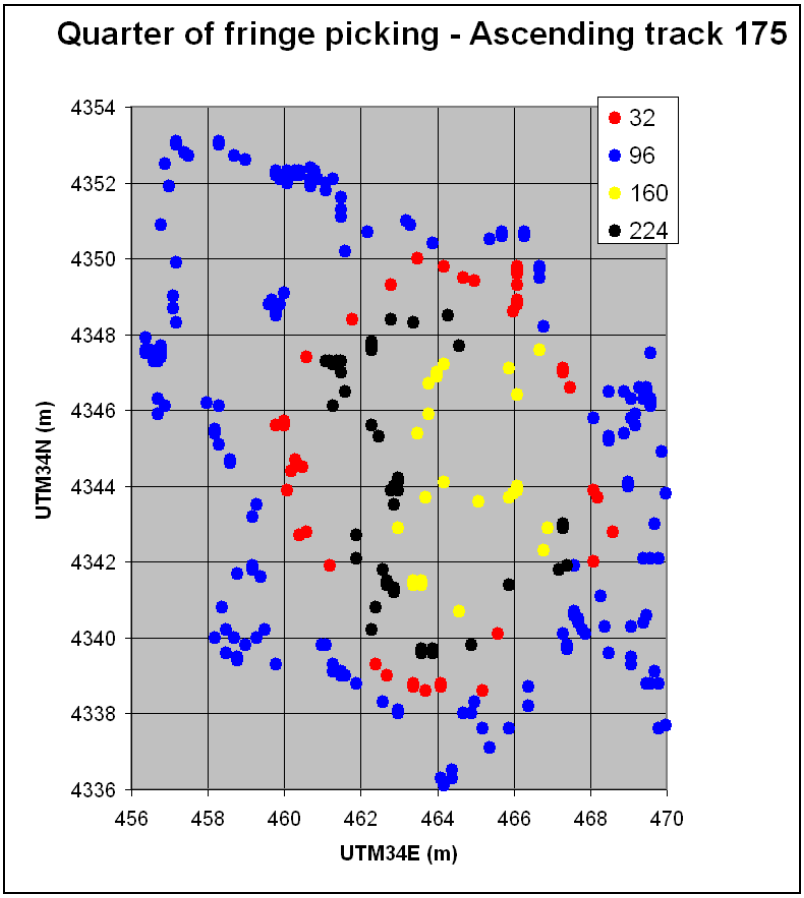

270

Preprints (www.preprints.org) | NOT PEER-REVIEWED | Posted: 27 August 2020 doi:10.20944/preprints202008.0590.v1

Figure 7. Location of the picked fringes on the descending (top) and ascending (bottom) interferogram. Ground deformation extends to approximately 14 km (E-W) and 17 km (N-S) for the ascending interferogram and it is much more localized for the ascending one.

3.3 Results of Inversion Modelling

Assuming a half-space elastic model with uniform slip along a rectangular fault surface, the source of the ground deformation was inverted using the InSAR data and the code *inverse6* [35]. For the modelling of the interferograms we gave the same weight to the ascending and descending data and the same zero value for the fringes. The question of the tuning of the zero values has been explained in the previous section. The equal weight is obtained by using the same number of ascending and descending observations, here 86 for both, thus 172 observations in total. The mean scatter between data and model is 3.3 mm for the 86-descending data (Fig. 8 top) and 3.9 mm for the 86-ascending data (Fig. 8 bottom). We assume that the seismic fault plane is the one with low-angle reverse fault dipping towards ENE. This is the most consistent with the geomorphology and the tectonic context of the area.

We invert for the 3D coordinates of the fault-top centre and for the fault length. We do not invert for the strike, dip and rake angles, assuming 329°, 39° and 102° respectively, *i.e.* using the average values of the various determinations of the focal mechanism parameters (see Tab. 3). The dip angle is, among the three angles, the one that is less constrained. For the two other angles there is a trade-off between strike and rake. We tested models with the strike and/or the rake free but we could not constrain well those parameters. This was expected given the almost circular shape of the interferograms, especially the ascending one (Fig. 6).

In a first series of inversions we find that the width of the fault has the tendency to become large, between 4.5 and 6 km and the length small, between 4 and 5 km, with the surface area remaining almost constant. As the width is not well constrained, we fix it at 4.7 km, a value the leads to an equal length of 4.7 km, thus a square fault. We also released the amplitude of slip and rake: we found that the amplitude had the tendency to grow (*i.e.* from an initial 0.3 m to 0.6 m or more) and the rake to remain steady. In the second set of inversions we constrained the slip to be 0.5 m, as the standard scaling laws (i.e. [36]) do not suggest a higher value for this earthquake, given also the size of the fault. The best fitting values for the four free parameters are reported in Tab. 7.

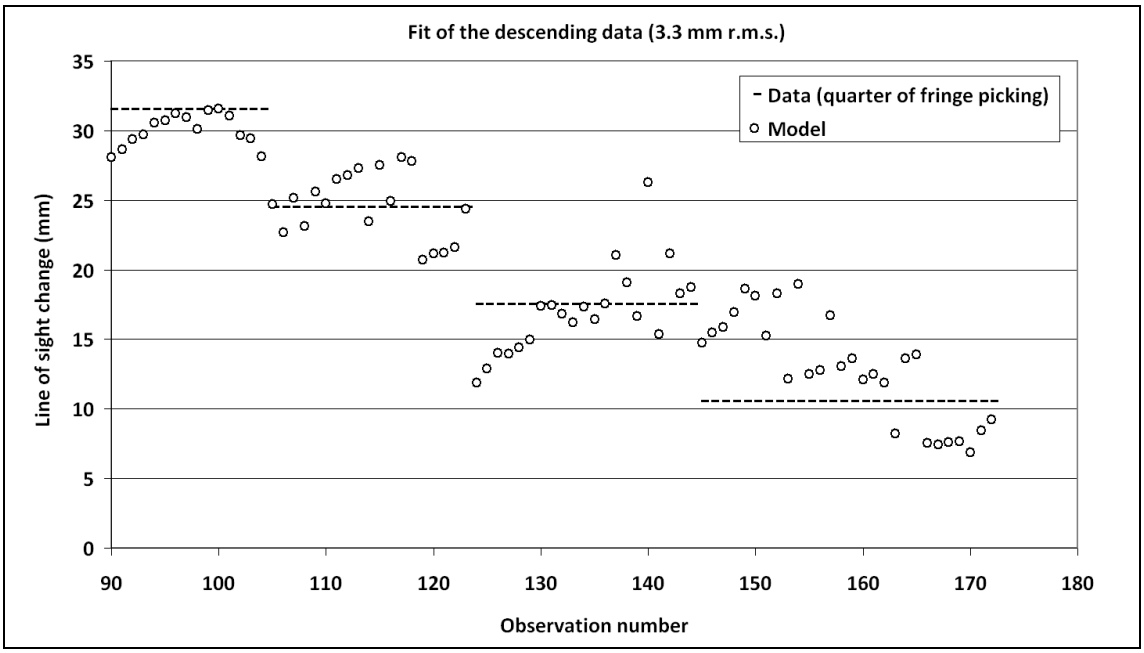

Preprints (www.preprints.org) | NOT PEER-REVIEWED | Posted: 27 August 2020 doi:10.20944/preprints202008.0590.v1

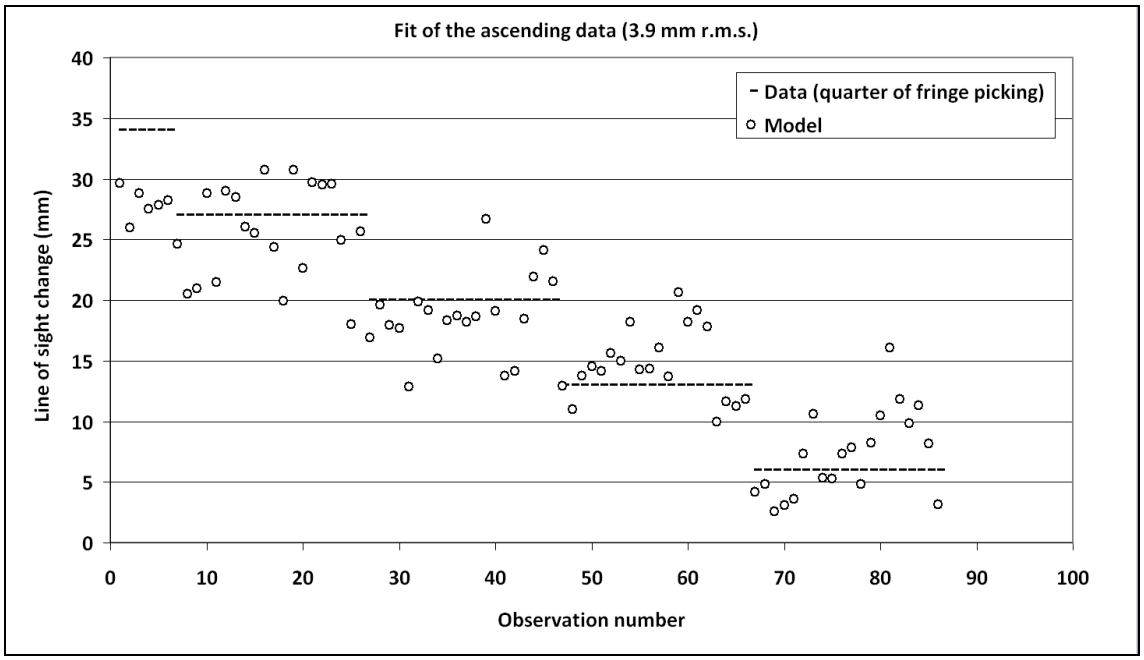

Figure 8. Scatterplots showing fit of the data to the reverse fault model (open circles). The mean scatter between data and model is 3.3 mm for the 86-descending data (top) and 3.9 mm for the 86-ascending data (bottom). The numerical values are in the Supplementary text S2.

Table 7. Parameters of the best fitting fault model assuming fixed values for strike=329°, dip=39°, rake=102° and fault width=4.7 km. The fault tip is located at 7 km depth.

Centre of upper edge of the fault			**Fault length**
East	North	Vertical	
UTM34 (km)	UTM34 (km)	km	km
464.76	4344.28	7.0	4.7

4. Discussion

4.1 Characteristics of the Kanallaki seismic fault

Fig. 9a shows the surface projection of the seismic fault and Fig 9b a cross section, oriented NE-SW. The upper edge of the fault is located at a depth of 7.0 km, beneath the village of Kanallaki. The mid-point of the top-fault is located at 20.59°E, 39.25°N and the geodetic centroid is 8.5 km depth. The fault length is 4.7 km (Tab. 7). The geodetic seismic moment, assuming a rigidity of $3 \bullet 10^{10}$ Pa for the upper crust is $3.31 \bullet 10^{17}$ N m. This is within the range of values found from seismology (Tab. 3) and close to the NOA-revised ($2.86 \bullet 10^{17}$ N m; Tab. 3) so it is consistent. The slip inferred from our model (0.5 m) is twice larger that the theoretical slip predicted by the scaling laws of [37] (0.26 m). Those scaling laws predict a fault length of 6.4 km and a fault width of 6.46 km, respectively. In our case the length is very well constrained by the fringes and cannot grow above a maximum of 5 km (4.7 km in our best fitting model) while the width, which is not very well constrained could grow up to 6 - 6.5 km. Accepting such unusual elongated shape for the fault would allow reducing the amplitude of the slip, for example a fault of 4.5 x 6.5 km and slip of 0.38 m would fit the interferogram equally well with better consistency with the scaling laws. We prefer to retain a square geometry for the seismic source primarily because it comprises a continental thrust with a dip-angle of ~39° and b) the map view of aftershocks (Fig. 3b) does not show a NE-SW distribution which would be in favour of an increased fault-width.

Preprints (www.preprints.org) | NOT PEER-REVIEWED | Posted: 27 August 2020 doi:10.20944/preprints202008.0590.v1

Fig. 9b presents, with the same horizontal and vertical scale, a 19 km long cross section of the Kanallaki area running from the shore towards the interior, perpendicular to the strike of the fault (passing through the geodetic centroid). In this section we show the topography in blue and the vertical deformation (surface uplift) in red, as deduced from our fault model (Tab. 7). The maximum value of the vertical displacement is +4 cm at the abscissa 9.71 km, i.e. almost on top of the location of the upper tip of the fault (abscissa 8.9 km), that is on its hanging wall side.

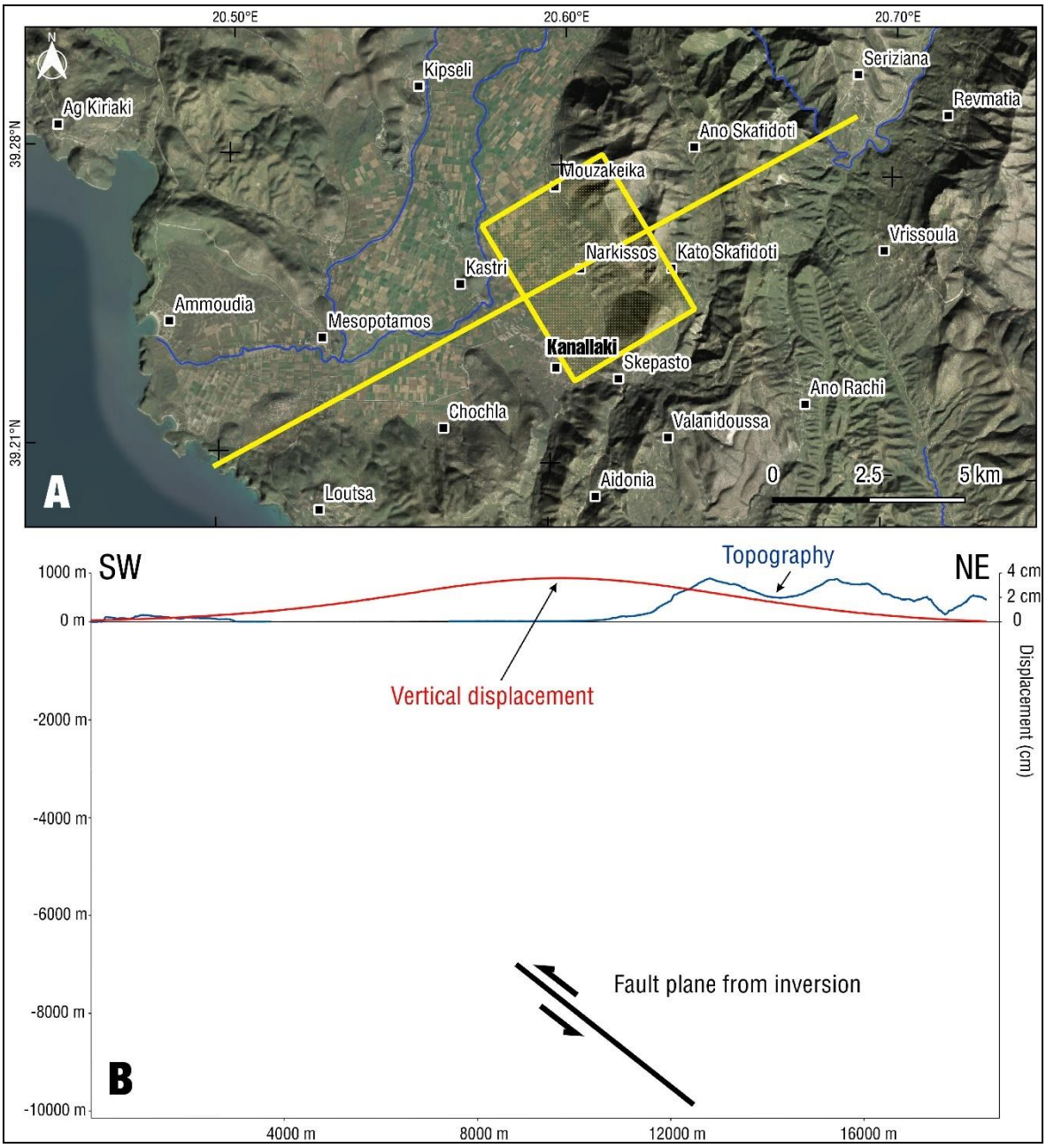

Figure 9. Map (a) showing surface projection of the fault plane (yellow rectangle; length 4.7 km, width 4.7 km), b) Location of the fault (black line with arrows indicating the relative motion of the two blocks) inferred from the modelling of the descending interferogram. The scale is the same in both horizontal and vertical axes and the topography is not exaggerated.

Fig. 10 shows a simplified geological map and a structural section of the crust beneath Kanallaki. The 21 March 2020 earthquake has presumably occurred in one of the two main reverse-slip structures of Margariti and Parga, outcropping in the area. The thrust fault of Margariti (code GR0695 on the NOAFault database; [38], https://arcg.is/04Haer) continues south towards

Preprints (www.preprints.org) | NOT PEER-REVIEWED | Posted: 27 August 2020 doi:10.20944/preprints202008.0590.v1

Loutsa (Fig. 9a; following [39]) and possibly offshore. It may root into the basal decollement of the Ionian zone over the crystalline basement. There are also Triassic evaporitic outcrops near Margariti (Fig. 10a) and Loutsa that imply the existence of a major thrust there. As the Margariti thrust fault (see Fig. 4) is more than 12-km long its down-dip extension could reach the Kanallaki area (Fig. 10), ~10 km to the east, and such a geometry complies also with the geodetic centroid depth of 8.5 km that we obtained for the 2020 seismic fault.

To the northwest of Kanallaki and west of Gardiki (Fig. 10a), the Lippa mountain forms a ~400 m high N-S anticline composed of hard carbonate rocks of the Ionian zone. The Kokitos and Acherontas rivers reach the sea south of this anticline (Fig. 9a; see Fig. S5 for an aerial view; other sub-parallel anticlines also exist). Whether the Lippa mountain structure is part of the active thrust system that roots at the decollement of 7-8 km depth requires further investigations (seismic profiles and drilling). In such case, the growth of the anticline would be balanced by erosion that is removed by the two rivers. On-going tectonic activity is also evidenced by uplift of the Epirus coastline due to the Late Tertiary convergence between the Apulian block and Eurasia [12].

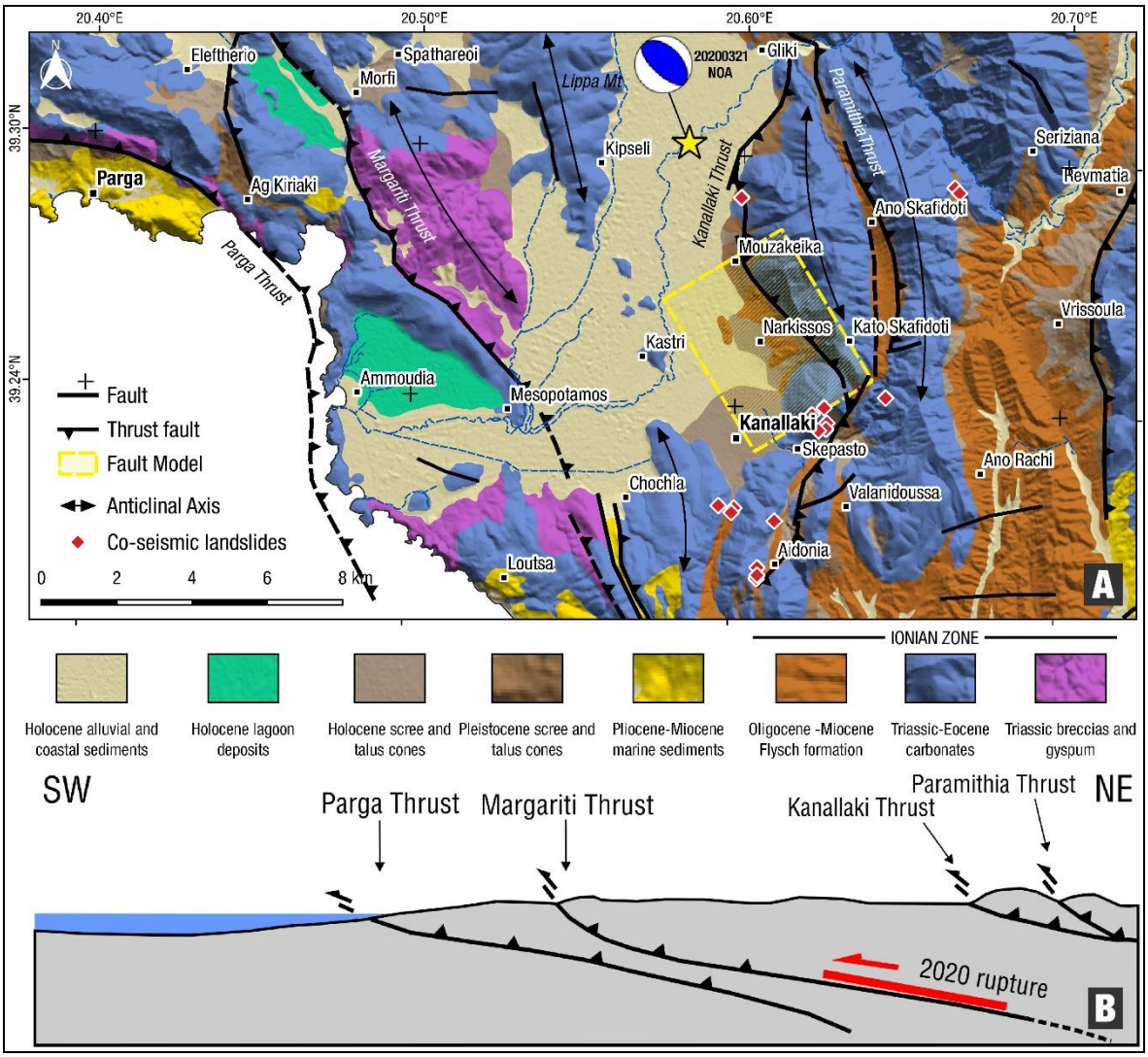

Figure 10 a): Simplified geological map, modified after [14,16,40]. Red diamonds mark the locations of co-seismic landslides for the March 21 2020 earthquake, identified using Sentinel-2 optical imagery (see Table S4 for coordinates). b): simplified section (not to scale) of the crustal structure beneath the Parga-Kanallaki area (azimuth of the section N245°E). Red line (with arrow on the overthrusting side) indicates the seismic fault.

Preprints (www.preprints.org) | NOT PEER-REVIEWED | Posted: 27 August 2020 doi:10.20944/preprints202008.0590.v1

4.2 Tectonic strain and the determination of the deformation zone west of Kanallaki

We analyzed new GNSS data of the Greek permanent stations in Epirus and north Ionian Sea (Corfu and Paxoi islands; Tab. 8). The GNSS stations belong to the NOANET geodetic network [41,42], the Hexagon SmartNet and the Uranus commercial network (see Fig. 1 for locations). The processing was made with the Precise Point Positioning (PPP) strategy [43] by means of the GIPSY/OASIS II software (ver. 6.4) developed by the Jet Propulsion Laboratory (JPL; http://gipsy-oasis.jpl.nasa.gov; [44]). We used the JPL final orbits (flinnR) and clocks, absolute antenna calibrations, random walk troposphere estimation, and the FES2004 ocean loading model. The tectonic velocities and uncertainties retrieved from the analysis of the time series are in Tab. 8.

Tab 8. Velocities of several permanent GPS stations located in north-western Greece (Fig. 1b) with longitude between 19°-21° and latitude between 39°-40°. The velocities are plotted in Fig. 12 (with respect to rigid Apulia) and Fig. 13 (w.r.t. station GARD). See Fig. 1 for locations.

Site	Network	Long	Lat	vE	vN	vE_ Apulia	vN_ Apulia
		°	°	mm yr^{-1}	mm yr^{-1}	Mm yr^{-1}	mm yr^{-1}
KERK	HxSmart	19.8734	39.4937	21.1 ± 0.3	14.7 ± 0.3	-4.0	-3.7
KERU	Tree	19.9152	39.6191	22.1 ± 0.4	14.5 ± 0.4	-3.0	-3.9
KASI	NOA	19.9355	39.7464	20.3 ± 0.3	14.0 ± 0.3	-4.8	-4.4
PAXO	HxSmart	20.1639	39.2108	24.3 ± 0.4	16.4 ± 0.4	-0.8	-2.0
IGOU	HxSmart	20.2627	39.5100	21.2 ± 0.4	13.6 ± 0.3	-3.9	-4.8
HGOU	Tree	20.2679	39.4927	21.3 ± 0.4	14.2 ± 0.4	-3.8	-4.2
GARD	Tree	20.5710	39.3506	21.1 ± 0.4	13.2 ± 0.5	-4.0	-5.2
IOAN	HxSmart	20.8505	39.6641	21.7 ± 0.3	11.0 ± 0.3	-3.4	-7.4
IOAU	Tree	20.8541	39.6549	22.0 ± 0.5	10.2 ± 0.4	-3.1	-8.2
ART1	HxSmart	20.9333	39.1529	17.3 ± 0.6	9.1 ± 0.6	-7.8	-9.3
ARTA	HxSmart	20.9917	39.1588	18.7 ± 0.3	10.8 ± 0.3	-6.4	-7.6

The long-term N-S velocities, in the reference frame ITRF2014, are increasing from south (ARTA; 10.8 ± 0.3 mm yr^{-1}) to north (KASI; 14.0 ± 0.3 mm yr^{-1}) while the E-W velocities show a "plateau" at 20.3-22.1 mm yr^{-1} (the two ARTA stations show lower rates). The station velocities near Arta (Fig. 1) also reflect the N-S extension of the Amvrakikos graben [11,45,46], so they will be left out in further analysis. Another notable exception in this kinematic field is the Hexagon-SmartNet station PAXO (Fig. 1) whose E-W velocity is 24.3 ± 0.4 mm yr^{-1} and was also considered in the strain analysis made by [11].

Using the velocities of Tab. 8 we calculate the convergence towards Apulia in the azimuth N228°E which is the azimuth that fit best the vectors of the stations located close to the coast (thus excluding the two stations of Ioannina). We note that the orientation of the coast is globally perpendicular to this azimuth. The values of the convergence and their uncertainties are presented in Tab. 9. The convergence of PAXO towards Apulia is of 1.9 ± 0.4 mm yr^{-1}. For the three stations of Corfu (KASI, KERK, KERU; Fig. 1) the average convergence towards Apulia is 5.6 ± 0.4 mm yr^{-1} (in the azimuth N228°E). For the two stations of Igoumenitsa (IGOU, HGOU) the average convergence is 5.8 ± 0.4 mm yr^{-1}, close to the value of Corfu. For GARD the rate it is 6.5 ± 0.45 mm yr^{-1}. For the two stations of Ioannina (IOAN, IOAU) the average convergence is 7.6 ± 0.4 mm yr^{-1}. As the net rate of convergence between Apulia and stable Europe in only 5.2 mm yr^{-1} (considering stations across the Adriatic Sea), we see that the convergence is amplified in northwest Greece. This is due to the compression and rotation imposed by the westward component of movement of the Anatolian micro-plate towards Apulia, a process that can be perceived until the south of Albania [11,12]. It is

Preprints (www.preprints.org) | NOT PEER-REVIEWED | Posted: 27 August 2020 doi:10.20944/preprints202008.0590.v1

noteworthy that the shortening rate of the crust between the Epirus coastal GNSS stations and station PAXO in the Ionian Sea is equivalent to 4.6 mm yr^{-1} or ~50% of the overall convergence.

Table 9. Values of the convergence rate of the stations of Epirus with Apulia using the azimuth N228°E for the convergence axis.

Station	Convergence towards Apulia mm yr^{-1}	Uncertainty mm yr^{-1}
KERK	5.4	0.3
KERU	4.8	0.4
KASI	6.5	0.3
PAXO	1.9	0.4
IGOU	6.1	0.4
HGOU	5.6	0.4
GARD	6.5	0.5
IOAN	7.5	0.3
IOAU	7.8	0.5

By modelling this convergence with a simple back-slip model in elastic half-space (Fig. 11) we find the best fit for a total convergence rate of 8.9 mm yr^{-1}, thus an extra compression of 3.7 mm yr^{-1} that is recovered in the regions located to the east and north of Ioannina. The modelled central axis of the convergence band, with azimuth N318°E, passes along the southwest coast of Corfu, along the northeast coast of Paxos, heading toward the northern extremity of the Lefkada island (Fig. 12). The extent of the deforming area (box in Fig. 12), when defined as the band that accommodates 80% of the total convergence, is 60 km, with a best fitting locking depth of 11 km. Unfortunately, the limited surface displacement data are not dense enough to allow for a formal inversion so as to recover the slip deficit patterns along the deformation front.

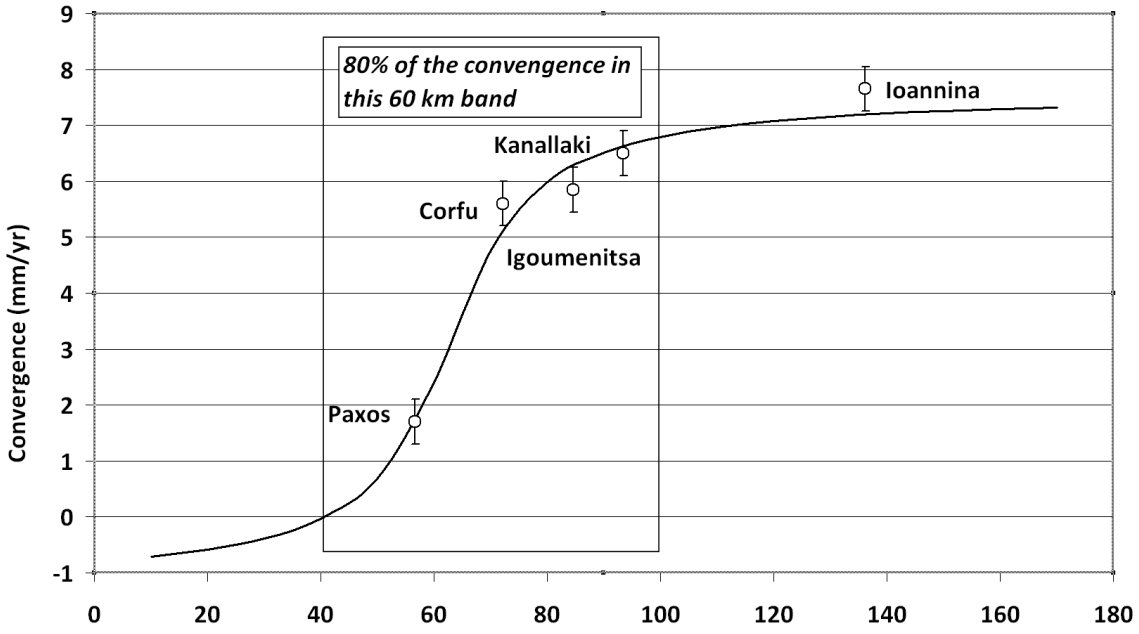

Figure 11. Graph showing convergence rate (in mm/yr) with respect to the Apulian block along a profile oriented N228°E.

Preprints (www.preprints.org) | NOT PEER-REVIEWED | Posted: 27 August 2020 doi:10.20944/preprints202008.0590.v1

Therefore, PAXO appears to be located already slightly on the Apulian side of the deforming zone, while it is exactly the opposite for the stations onshore Corfu (KASI, KERK, KERU), with the axis of the plate boundary zone with Africa passing close to both islands and continuing along the coast of Albania. Between Corfu and Epirus (the Igoumenitsa stations IGOU - HGOU) the data and the model (Fig. 11) show that there is no significant shortening within the velocity uncertainties of ± 0.2 mm yr^{-1}, confirming the conclusions of [42}.

It is noteworthy that there is a 120 ns yr^{-1} active shortening of the crust between the two GNSS stations PAXO and GARD located at 38 km one to the other, and roughly in the ENE-WSW direction (N246°E). This 1-D estimate of tectonic strain is about 2.4 times larger than the 2-D estimates from regional studies, e.g. the 50 ns yr^{-1} found by [11] possibly because of the strong smoothing effect of the regional strain calculations of [11]. In addition, both Ioannina GNSS stations (IOAN, IOAU) exhibit long-term shortening of 41 and 51 ns yr^{-1} with respect to GARD, respectively (Fig. 13), indicating on-going compression onshore Epirus, yet decreasing significantly when moving away from the collision front.

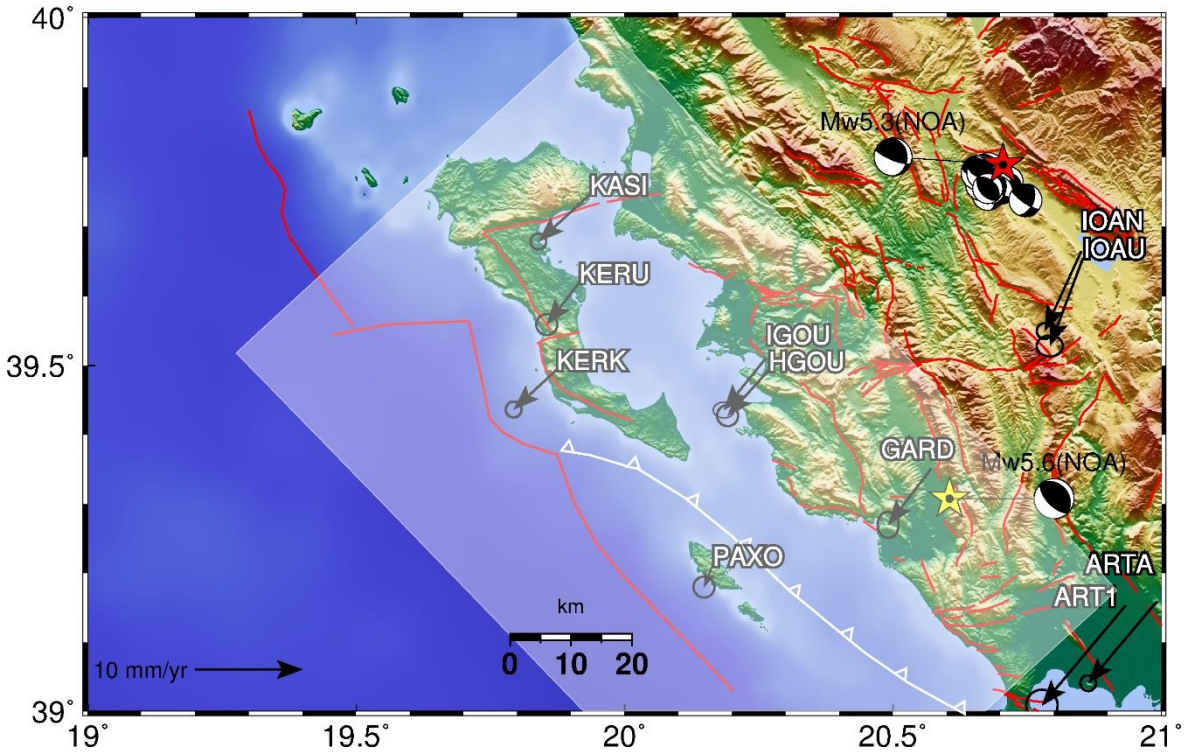

Figure 12. GNSS station velocities with respect to the Apulian block, assuming an ITRF2014 velocity of 25.1 mm yr^{-1} and 18.4 mm yr^{-1} for this Apulian block at the coordinate 20.0°E, 39.5°N (error ellipses are at 95% confidence interval). The shaded rectangle denotes the wide deformation zone along the Apulia-Eurasia collision front, determined at this study. Beachballs indicate focal mechanisms referring to the 2016 Ioannina event (red star) and the 2020 Kanallaki event (yellow star; NOA database (https://bbnet.gein.noa.gr/HL/index.php). White line between Paxos island and Corfu indicates the trace of the Ionian thrust (ticks on the overriding side).

4.3 On the regional extent of on-going compression in Epirus and the significance of the Ioannina 2016 compressional event

Preprints (www.preprints.org) | NOT PEER-REVIEWED | Posted: 27 August 2020 doi:10.20944/preprints202008.0590.v1

Unlike the shallow depth of the Kanallaki event, the M_{NOA} = 5.3 October 15, 2016 20:14 UTC Ioannina thrust earthquake [47,48,49] (Fig. 12) had a depth of 14 km, while maintaining similar kinematics. The earthquake occurred 20 km to the NW of Ioannina, Epirus, NW Greece, at an area where microseismicity had already been detected by [6]. The main shock was followed by a few hundreds of aftershocks in the period up to October 25, 2016. The hypocentre (14 km depth) is located inside the pile of deformed carbonates of the Ionian zone of the Hellenides and close to the crystalline basement. Because of the concern for Ioannina we made Sentinel differential interferograms immediately after that event but we saw no deformation. This is because the moderate-size event was too deep. Also, GPS data processing showed no displacement at the two stations of Ioannina (Fig. 1). Analysis of the moment tensor solution of the earthquake and its stronger aftershocks (Fig. 13) and map distribution of aftershocks revealed seismic slip along a shallow, east-dipping (27°) reverse fault, striking NNW-SSE [49]. That earthquake signifies the change in the stress-field near the meridian 20.8°E from N-S extension (Pindos mountains) to E-W shortening near Ioannina [11]. The deep setting of the thrust fault inside the Ionian fold-and-thrust belt of the external Hellenides denotes the on-going accommodation of brittle deformation about 80 km to the east of the collision front with Apulia (Fig. 13).

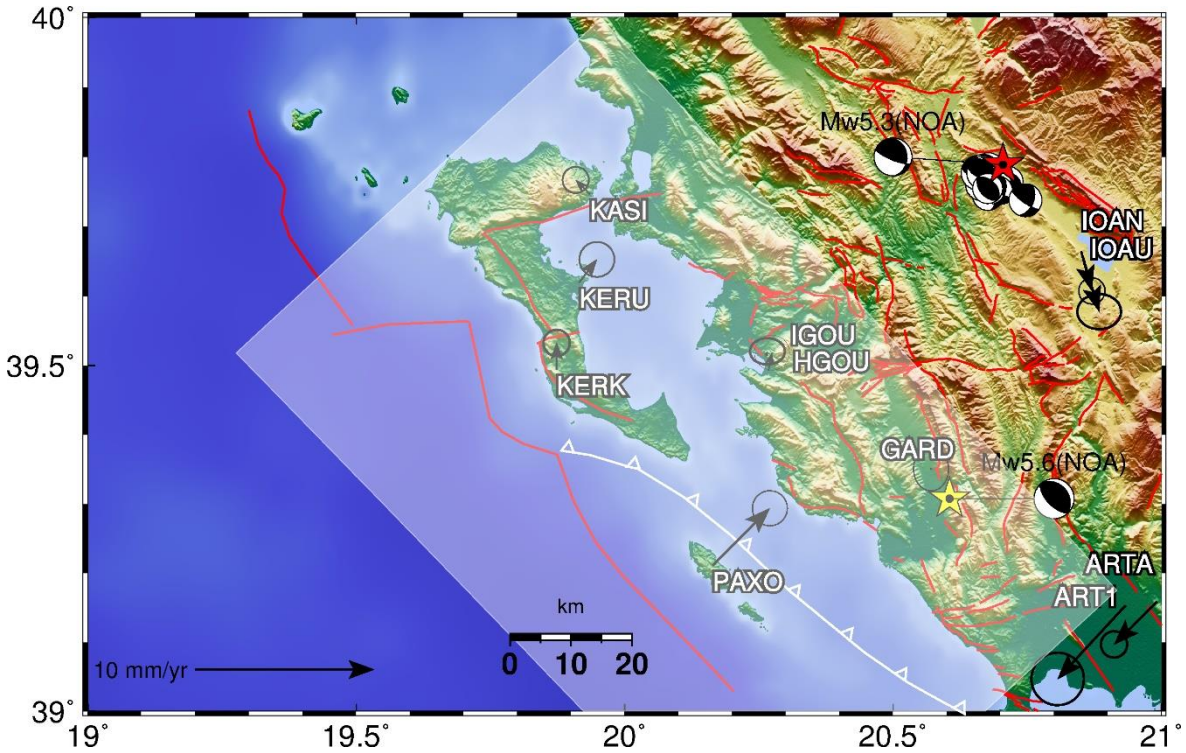

Figure 13. Velocity of the GPS stations around Kanallaki, assigning zero motion to GARD. The shaded rectangle denotes the wide deformation zone along the Apulia-Eurasia collisional front, determined at this study. Beachballs indicate focal mechanisms referring to the 2016 Ioannina event (red star) and the 2020 Kanallaki event (yellow star; NOA database (https://bbnet.gein.noa.gr/HL/index.php). White line between Paxos island and Corfu indicates the trace of the Ionian thrust (ticks on the overriding side).

5. Conclusions

1. We identify the main source of the Mw = 5.6 earthquake that hit western-central Epirus on March 21, 2020 to be located on the Margariti thrust fault, within the frontal area of the Ionian fold and thrust belt of the Hellenic orogen.

2. We modelled the seismic fault by combining the ascending and descending Sentinel-1 observations. We find that we can model the overall fringe pattern by reverse slip on an east-dipping fault. The fault plane is a low-angle thrust fault (~5 by 5 km) that dips 39° towards east.
3. The inversion of geodetic data suggests that the upper edge of the fault is at a depth of 7 km, well constrained by the modelling of the interferograms.
4. InSAR shows ground motion towards the southwest and surface uplift in agreement with moment tensor solutions from seismology.
5. The damage distribution of the 14 May 1895 M=6.3 earthquake is compatible with a reverse-slip rupture along the Margariti thrust.
6. GNSS data indicate that the extent of the deforming crustal area between Apulia-Epirus (approximately Paxos-Kanallaki), accommodating 80% of the total convergence, is 60 km, with a best fitting locking depth of 11 km.
7. The island of Paxos appears to be already on the Apulian side of the deforming zone, while it is exactly the opposite for the GNSS stations onshore Corfu (KASI, KERK, KERU; Fig. 11), with the axis of the plate boundary zone between Africa passing close to both islands and continuing along the coast of Albania.

Supplementary Materials: The following are available online at www.mdpi.com/xxx/s1, Figure S1: Results of the ISOLA modelling of the mainshock, Figure S2: Map of the relocated 2020 Kanallaki earthquake sequence, Figure S3: Map showing the Sentinel-1 frames with data used in this paper, Figure S4: Coseismic interferograms for the Kanallaki earthquake that were not used in the inversion due to low quality and noise, Figure S5: Aerial overview of the earthquake epicentre area, Table S1: Catalogue of strong events for the study area, 1915 - 2019, Table S2: Observed values (fringe picking) and modelled values, Table S3: Variability of the solution as a function of the focal mechanism parameters, Table S4: Location of co-seismic landslides identified using Sentinel-2 images for the Mw 5.6 March 23 2020 earthquake.

Author Contributions: For research articles with several authors, a short paragraph specifying their individual contributions must be provided. The following statements should be used "Conceptualization, S.V, A.G. and P.B.; methodology, P.B and P.E.; software, S.V, P.E, V.K and V.T.; validation, S.V, P.P and A.G; formal analysis, P.B, V.K and P.E; investigation, A.G, S.V, V.T, A.F and H.P.; resources, S.V, P.P and A.G; data curation, P.B, V.T, A.F and H.P.; writing—original draft preparation, S.V, P.B and A.G.; writing—review and editing, all authors.; visualization, S.V, V.K and P.E.; supervision, A.G and P.B.; funding acquisition, A.G. All authors have read and agreed to the published version of the manuscript.".

Funding: Athanassios Ganas thanks "HELPOS - Hellenic Plate Observing System" (MIS 5002697) which is funded by the Operational Programme "Competitiveness, Entrepreneurship and Innovation" (NSRF 2014-2020) and co-financed by Greece and the European Union (European Regional Development Fund).

Acknowledgments: We thank Efthimios Lekkas, Efthimios Sokos, Hélène Lyon-Caen, Nicolas Chamot-Rooke, Ioannis Kassaras, Ioannis Karamitros and Christos Papaioannou for discussions. We thank ESA, Geohazards Lab and Terradue for providing access to Geohazards Exploitation Platform (GEP) for InSAR cloud processing. GNSS data were provided by NOANET, Hexagon SmartNET and Uranus (Tree) networks of Greece. Seismic Waveform data were sourced from the corresponding ORFEUS EIDA node operated by the National Observatory of Athens (eida.gein.noa.gr). We thank the NOA analysis team for their phase data. We used data from the HL (Institute of Geodynamics, National Observatory of Athens, doi: 10.7914/SN/HL), HP (University of Patras, doi: 10.7914/SN/HP), which is cooperating certain stations jointly with the Charles University in Prague, HT (Aristotle University of Thessaloniki, doi: 10.7914/SN/HT), HA (National and Kapodistrian University of Athens, doi: 10.7914/SN/ HA), and HI (Institute of Engineering Seismology and Earthquake Engineering, doi: 10.7914/SN/HI) networks. The ALOS Global Digital Surface Model - 30 m is available from https://www.eorc.jaxa.jp/ALOS/en/aw3d30/index.htm. We thank the QGIS Development Team - Open Source Geospatial Foundation Project http://qgis.osgeo.org.

Conflicts of Interest: The authors declare no conflict of interest.

References

1. Underhill, J.R. Late Cenozoic deformation of the Hellenide foreland, western Greece. *GSA Bulletin* **1989**, 101 (5), 613-634.
2. King, G.; Sturdy, D.; Whitney, J. The landscape geometry and active tectonics of northwest Greece. *GSA Bulletin* **1993**, 105, 137-161.
3. Karakitsios, V. Western Greece and Ionian Sea petroleum systems. AAPG Bulletin 2013. 97 (9), 1567-1595.
4. Handy, M. R.; Giese, J.; Schmid, S. M.; Pleuger, J.; Spakman, W.; Onuzi, K.; Ustaszewski, K. Coupled crust-mantle response to slab tearing, bending, and rollback along the Dinaride-Hellenide orogen. *Tectonics* **2019**. 38 (8), 2803-2828.
5. Olive, J-A.; Pearce, F.; Rondenay, S; Behn, M.D. Pronounced zonation of seismic anisotropy in the Western Hellenic subduction zone and its geodynamic significance. *Earth and Planetary Science Letters* **2014**. 391, 100-109.
6. Hatzfeld, D.; Kassaras, I.; Panagiotopoulos, D.; Amorese, D.; Makropoulos, K.; Karakaisis, G.; Coutant, O. Microseimicity and strain pattern in northwestern Greece. *Tectonics* **1995**. 14 (4), 773-785.
7. Baker, C.; Hatzfeld, D.; Lyon-Caen, H.; Papadirnitriou E.; Rigo, A. Earthquake mechanisms of the Adriatic Sea and Western Greece: implications for the oceanic subduction-continental collision transition. *Geophys. J. Int.* **1997**. 131, 559-594
8. Louvari, E.; Kiratzi, A.; Papazachos, B.; Hatzidimitriou, P. Fault-plane solutions determined by waveform modeling confirm tectonic collision in the eastern Adriatic, Pure Appl. Geophys. 2001. 158, 1613-1637.
9. Tselentis, G.A.; Sokos, E.; Martakis, N.; Serpetsidaki, A. Seismicity and seismotectonics in Epirus, western Greece: results from a microearthquake survey. *Bulletin of Seismological Society of America* **2006**. 96 (5), 1706-1717
10. Pérouse, E. ; Chamot-Rooke, N. ; Rabaute, A. ; Briole, P. ; Jouanne, F. ; Georgiev, I. ; Dimitrov, D. Bridging onshore and offshore present-day kinematics of central and eastern Mediterranean: Implications for crustal dynamics and mantle flow. *Geochem. Geophys. Geosyst.* **2012**. 13, Q09013.
11. D'Agostino, N.; Métois, M.; Koci, R.; Duni, L.; Kuka, N.; Ganas, A.; Georgiev, I.; Jouanne, F.; Kaludjerovic, N.; Kandić, R. Active crustal deformation and rotations in the southwestern Balkans from continuous GPS measurements. *Earth and Planetary Science Letters* **2020**. 539, 116246.
12. van Hinsbergen, D.J.J.; van der Meer, D.G.; Zachariasse, W.J.; et al. Deformation of western Greece during Neogene clockwise rotation and collision with Apulia. *Int. J. Earth Sci. (Geol. Rundsch.)* **2006**. 95, 463.
13. Zelilidis, A.; Piper, D.J.W.; Vakalas, I.; Avramidis, P.; Getsos, K. Oil and gas plays in Albania: Do equivalent plays exist in Greece? *Journal of Petroleum Geology* **2006**, 26 (1), 29–48.
14. IGRS-IFP. *Etude Géologique de l' Epire (Grèce nord-occidentale)*. Editions Technip, Paris, France, 1966 pp 306.
15. Monopolis, D.; Bruneton, A. Ionian Sea (western Greece): Its structural outline deduced from drilling and geophysical data. *Tectonophysics* **1982**, 83, 227–242.
16. Paschos, P.; Rondoyianni, T. ; Mettos, A. *Neotectonic Map of Greece in Scale 1:100000, Map Sheet Arta*. Institute of Geology and Mineral Exploration, Athens, Greece 2011.
17. Ntokos, D. Neotectonic study of Northwestern Greece. *Journal of Maps* **2018**. 14(2), 178-188.
18. Lekkas, E.; Mavroulis, S.; Carydis, P.; Skourtsos, E.; Kaviris, G.; Paschos, P.; Ganas, A.; Kazantzidou-Firtinidou, D.; Parcharidis, I.; Gatsios, T.; Angelou, D.; Karavias, A.; Bafi, D.; Markogiannaki, O. *The March 21, 2020, Mw 5.7 Epirus (Greece) Earthquake*. Newsletter of Environmental, Disaster and Crises Management Strategies, Department of Geology and Geoenvironment, National and Kapodistrian University of Athens, 17, ISSN 2653-9454 https://edcm.edu.gr/images/docs/newsletters/Newsletter_17_2020_Epirus_EQ.pdf
19. Sokos E.N.; Zahradnik J. ISOLA a Fortran code and a Matlab GUI to perform multiple-point source inversion of seismic data. *Computers & Geosciences* **2008**. 34, 967–977.
20. Haslinger, F.; Kissling, E.; Ansorge, J.; Hatzfeld, D.; Papadimitriou, E.; Karakostas, V.; Makropoulos, K.; Kahle, H.-G.; Peter, Y. 3D crustal structure from local earthquake tomography around the Gulf of Arta (Ionian region, NW Greece). *Tectonophysics* **1999**. 304, 201–218.
21. Karakonstantis, A. 3-D Simulation of Crust and Upper Mantle Structure in the Broader Hellenic Area Through Seismic Tomography. PhD Thesis, Department of Geophysics-Geothermics, Faculty of Geology, University of Athens, Greece 2017. (*in Greek*)
22. Wadati, K. On the travel time of earthquake waves. Part. II. *Geophysical Magazine* **1933**. 7, 101–111.
23. Waldhauser, F. hypoDD - A Program to Compute Double-Difference Hypocenter Locations. *U.S. Geol. Surv. Open File Rep.*, 01-113, 2001. pp 25.

24. Papazachos, B.; Papazachou, C. *The earthquakes of Greece*, Editions Ziti, Thessaloniki, 1997.
25. Ambraseys, N. *Earthquakes in the Mediterranean and Middle East: a multidisciplinary study of seismicity up to 1900*. Cambridge University Press, 2009. pp 970.
26. Makropoulos, K.; Kaviris, G.; Kouskouna, V. An updated and extended earthquake catalogue for Greece and adjacent areas since 1900. *Nat. Hazards Earth Syst. Sci.* **2012**. 12, 1425-1430.
27. Kontoes, C.; Elias, P.; Sykioti, O.; Briole, P.; Remy, D.; Sachpazi, M.; Veis, G.; Kotsis, I. Displacement field and fault model for the September 7, 1999 Athens Earthquake inferred from ERS2 Satellite radar interferometry. *Geophys. Res. Lett.* **2000**. 27, 3989–3992.
28. Atzori S.; Manunta, M.; Fornaro, G.; A. Ganas, A.; Salvi, S. Postseismic displacement of the 1999 Athens earthquake retrieved by the Differential Interferometry by Synthetic Aperture Radar time series. *Journal of Geophysical Research* **2008**. 113, B09309.
29. Briole, P.; Elias, P.; Parcharidis, O.; Bignami, C.; Benekos, G.; Samsonov, S.; Kyriakopoulos, C.; Stramondo, S.; Chamot-Rooke, N.; Drakatou, M.L.; Drakatos, G. The seismic sequence of January–February 2014 at Cephalonia Island (Greece): constraints from SAR interferometry and GPS. *Geophysical Journal International* **2015**. 203 (3), 1528–1540.
30. Ilieva, M.; Briole, P.; Ganas, A.; Dimitrov, D.; Elias, P.; Mouratidis, A.; Charara, R. Fault plane modelling of the 2003 August 14 Lefkada Island (Greece) earthquake based on the analysis of ENVISAT SAR interferograms. *Tectonophysics* **2016**. 693, 47-65.
31. Ganas, A.; Elias, P.; Bozionelos, G.; Papathanassiou, G.; Avallone, A.; Papastergios, A.; Valkaniotis, S.; Parcharidis, I.; Briole, P. Coseismic deformation, field observations and seismic fault of the 17 November 2015 M=6.5, Lefkada Island, Greece earthquake. *Tectonophysics* **2016**. 687, 210-222.
32. Ganas, A.; Elias, P.; Kapetanidis, V.; Valkaniotis, S.; Briole, P.; Kassaras, I.; Argyrakis, P.; Barberopoulou, A.; Moshou, A. The July 20, 2017 M6.6 Kos Earthquake: Seismic and Geodetic Evidence for an Active North-Dipping Normal Fault at the Western End of the Gulf of Gökova (SE Aegean Sea). *Pure and Applied Geophysics* **2019**. 176 (10), 4177-4211.
33. Ganas, A.; Elias, P.; Briole, P.; Cannavo, F.; Valkaniotis, S.; Tsironi, V.; Partheniou, E.I. Ground Deformation and Seismic Fault Model of the M6.4 Durres (Albania) Nov. 26, 2019 Earthquake, Based on GNSS/INSAR Observations. *Geosciences* **2020**. 10 (6), 210.
34. Goldstein, R. M.; Werner, C. L. Radar interferogram filtering for geophysical applications. *Geophys. Res. Lett.* **1998**. 25(21), 4035-4038.
35. Briole, P. *Modelling of earthquake slip by inversion of GNSS and InSAR data assuming homogenous elastic medium*. Zenodo 2017. http://doi.org/10.5281/zenodo.1098399
36. Wells, D.L.; Coppersmith, K.L. New Empirical Relationships among Magnitude, Rupture Length, Rupture Width, Rupture Area and Surface Displacement. *Bulletin of Seismological Society of America* **1994**. 84 (4), 974-1002.
37. Thingbaijam, K.K.S.; Martin Mai, P.; Goda, K. New empirical earthquake source-scaling laws. *Bulletin of Seismological Society of America* **2017**. 107 (5), 2225-2246.
38. Ganas, A. *NOAFAULTS KMZ layer Version 2.1*. Zenodo 2019. http://doi.org/10.5281/zenodo.3483136
39. Bacopoulos, I. *Lithostratigraphy of the Ionian basin in the southern part of Epirus related to the migration and entrapment of its hydrocarbons*. PhD Thesis, University of Athens, 2006. (*in Greek*)
40. Perrier, R.; Koukouzas, C. *Geological Map of Greece in scale 1:50000, Map Sheet Parga*. Institute of Geology and Mineral Exploration, Athens, 1969.
41. Ganas, A.; Drakatos, G.; Rontogianni, S.; Tsimi, C.; Petrou, P.; Papanikolaou, M.; Argyrakis, P.; Boukouras, K.; Melis, N.; Stavrakakis, G. NOANET: the new permanent GPS network for Geodynamics in Greece. *European Geophysical Union, Geophysical Research Abstracts* 2008. 10, EGU2008-A-04380.
42. Ganas, A.; Marinou, A.; Anastasiou, D.; Paradissis, D.; Papazissi, K.; Tzavaras, P.; Drakatos, G. GPS-derived estimates of crustal deformation in the central and north Ionian Sea, Greece: 3-yr results from NOANET continuous network data. *Journal of Geodynamics* **2013**. 67, 62– 71.
43. Zumberge, J.F.; Heflin, M.B.; Jefferson, D.C.; Watkins, M.M.; Webb, F.H. Precise point positioning for the efficient and robust analysis of GPS data from large networks. J. *Geophys. Res. Space Phys.* **1997**. 102, 5005–5017.
44. Bertiger, W.; Desai, S.D.; Haines, B.; Harvey, N.; Moore, A.W.; Owen, S.; Weiss, J.P. Single receiver phase ambiguity resolution with GPS data. *J. Geod.* **2010**. 84, 327–337.
45. Métois, M.; D'Agostino, N.; Avallone, A.; Chamot-Rooke, N.; Rabaute, A.; Duni, L.; Kuka, K.; Koci, R.; Georgiev, I. Insights on continental collisional processes from GPS data: Dynamics of the peri-Adriatic belts, *J. Geophys. Res. Solid Earth* **2015**. 120, 8701–8719.
46. Ntokos, D.; Lykoudi, E.; Rondoyanni, T. Geomorphic analysis in areas of low-rate neotectonic deformation: South Epirus (Greece) as a case study. *Geomorphology* **2016**. 263, 156-169.

47. ITSAK. *Preliminary report on the 15/10/2016 Ioannina M5.5 earthquake*. Institute of Engineering Seismology and Earthquake Engineering, Thessaloniki, Greece, 2016. pp 13. http://www.itsak.gr/uploads/news/earthquake_reports/EQ_Ioannina_20161015_M5.5.pdf (*in Greek*)
48. Pavlides, S.; Ganas, A.; Papathanasiou, G.; Valkaniotis, S.; Thomaidou, E.; Georgiadis, G.; Sboras, S.; Chatzipetros, A. *Geological-seismotectonic study of the wider area of Ioannina (seismic region of the earthquake October 15, 2016)*. Tectonics & Structural Geology Committee of the G.S.G., 1st TSG Meeting, Athens, 6 December 2016.
49. Pavlides S.; Ganas, A.; Chatzipetros, A.; Sboras, S.; Valkaniotis, S.; Papathanassiou, G.; Thomaidou, E.; Georgiadis, G. Geological and seismotectonic characteristics of the broader area of the October 15, 2016, earthquake (Ioannina, Greece). *European Geophysical Union, Geophysical Research Abstracts* 2017. 19, EGU2017-18135-1.